Journal of Ocean Engineering and Marine Energy (2021) 7:243–259
https://doi.org/10.1007/s40722-021-00200-3

RESEARCH ARTICLE

Numerical simulation of unsteady cavitating flow around 2-D MHKF-180 and NACA4418 hydrofoils

Srijna Singh[1] · **Mohammad Danish**[1] · **Kaushik Saha**[2]

Received: 10 November 2020 / Accepted: 20 May 2021 / Published online: 6 June 2021

Abstract

The low pressure regions on hydrofoils causes cavitation which results in a change of fluid dynamics characteristics. To understand the effect of cavitation on hydrofoil performance, a numerical study has been performed in this work using Zwart–Gerber–Belamri cavitation model and Realizable $\kappa-\epsilon$ turbulence model. Computations were performed for two-dimensional unsymmetrical MHKF-180 and NACA4418 hydrofoils. The performance of the hydrofoils at different angles of attack and cavitation numbers was studied based on the lift coefficient, drag coefficient, pressure coefficient and cavity length. The results of MHKF-180 were compared with that of NACA4418. From the comparison, it was found that under cavitating conditions the lift coefficient of MHKF-180 at different angles of attack is higher than NACA4418. Also, the cavity length on MHKF-180 is found to be smaller than that of NACA4418.

Keywords MHKF-180 · NACA4418 · Hydrofoil · Turbulence modeling · Cavitation modeling

List of symbols

c	Chord length of hydrofoil, m
Re	Reynold's number based on chord length
A	Area of hydrofoil, m^2
C_l	Lift coefficient
C_d	Drag coefficient
C_p	Pressure coefficient
l/d	Lift to drag ratio
u_i	Reynold's averaged velocity, m/s
U_∞	Freestream velocity, m/s
p	Local static pressure, Pa
p_v	Vapor pressure of liquid, Pa
p_∞	freestream pressure, Pa
R_e, R_c	Evaporation and condensation rate, $kg/(m^3\ s)$
α	Angle of attack, °
σ	Cavitation number
μ	Molecular viscosity, Pa s
μ_l	Viscosity of water, Pa s
μ_v	Viscosity of water-vapor, Pa s
μ_t	Turbulent viscosity, Pa s
μ_eff	Effective viscosity, Pa s
κ	Turbulent kinetic energy, m^2/s^2
ϵ	Rate of dissipation of turbulent kinetic energy, m^2/s^3
α_v	Vapor volume fraction
ρ_l	Liquid density, kg/m^3
ρ_v	Vapor density, kg/m^3
ρ_m	Mixture density, kg/m^3

1 Introduction

Cavitation, which is defined as a phenomenon of the formation of vapor bubbles in a liquid flow, has been a subject of intensive research because of its complex multiphase flow dynamics and the destruction it can do to the adjacent solid surfaces (Brennen 2014). Cavitation occurs in flow regions where the hydrodynamic effect reduces the local pressure below the saturation vapor pressure of the liquid, causing the formation of vapor bubbles. When these vapor bubbles enter the region of higher pressure, they collapse violently producing enough force to damage the solid body. Cavitation can be commonly seen around the propellers, hydrofoils, and

---

✉ Srijna Singh
ssrijna007@gmail.com

Mohammad Danish
mohammad.danish@bennett.edu.in

Kaushik Saha
kaushik.saha@ces.iitd.ac.in

[1] Department of Mechanical Engineering, Bennett University, Greater Noida, Uttar Pradesh 201310, India

[2] Centre for Energy Studies, IIT Delhi, New Delhi 110016, India

impellers in marine applications. In marine applications, the shape of the propellers is designed in a way that it can provide enough lift to keep the ship's hull on the water surface. The required lift can be achieved if the fluid on the top surface of the propeller flows at a higher velocity than its bottom surface, which in turn, reduces the pressure on the top surface (Štigler and Svozil 2009). However, the reduced pressure on the top surface makes it prone to cavitation.

In past, several theories were proposed to analyse the effects of cavitation on hydrofoils, some focusing on the analytical techniques, while others on the experimental observations and numerical simulations. Wu (1954) formulated the theory of finite span using lifting line theory to calculate the lift and drag force on the hydrofoil moving with constant velocity inside the incompressible and nonviscous liquid at a fixed depth. Fabula (1962) calculated the lift and drag force on the cavitating hydrofoil in steady incompressible flow as a function of cavitation number by applying the thin-airfoil theory and by conducting the experiment. He found good agreement between experimental and theoretical values. Woods (1964) extended the thin-airfoil theory to study the unsteady behaviour of cavitating and supercavitating flow on the two-dimensional hydrofoil and symmetrical wedge. Furuya (1975) also analysed the supercavitating hydrofoil, operating in the free surface to determine the gravity effect using three-dimensional non-linear free streamline theory and found that the shape of the cavity does not depend much on the gravity.

While some aspects of cavitation were successfully captured by the thin-airfoil theory, there was a need to further improve the understanding of cavitating flows, specifically in turbulent flows. For this purpose, Kermeen (1956) performed an experiment in high speed water tunnel on 3-D NACA4412 hydrofoil and modified circular arc, flat plate hydrofoil named Walchner profile 7. Lift force, pitching moment and drag force were calculated for both non-cavitating and cavitating flow. Lohrberg et al. (2002) performed numerical simulation on the cascade of two-dimensional hydrofoils with a semi-circular nose using the RNG $\kappa - \epsilon$ turbulence model. They found cloud cavitation on the topmost hydrofoil of the cascade while on the remaining two hydrofoils the sheet cavitation was observed. Through their simulation results, they had been able to determine the two dominant frequencies and their dependence on the cavitation number. These results were then complemented by the experiment that they conducted in a water tunnel. Billet and Holl (1981) conducted experiments on hydrofoil families consisting of NACA0015 and a cambered (asymmetrical about chord line) NACA0010. Through these experiments, they demonstrated the existence of other types of cavitation, like bubble ring cavitation, traveling cavitation, tip-vortex cavitation and sheet cavitation. Kubota et al. (1992) studied two-dimensional NACA0015 for experimental and numerical simulation at 8° and 20° angles of attack to develop Bubble Two-Phase Flow (BTF) model to understand the interaction between cavitation bubbles and viscous effects including large scale vortices. Kinnas and Fine (1993) analysed partial cavitation on 2D and 3D NACA16006 hydrofoils using BTF model and non-linear boundary element method (BEM) for two different cases. In the first case, length of cavity was determined for the known cavitation number while for the second case cavitation number was computed for the known cavity length. Comparing both models, they found that the BTF model has better convergence than the velocity-based BEM method.

In the above studies clearly, a large amount of experimental and numerical work have been reported related to flow around the NACA hydrofoils. The key quality observed in NACA44 series is its large leading radius providing advantage of good cavitation resistance (Phillips et al. 2012). While its sharp trailing edge leads to certain disadvantages when put in application like low structural efficiency, susceptibility to singing due to flexural vibration of the trailing edge. These vibrations are caused due to formation of vortices. These vortices are formed at a dominant frequency depending on water velocity and recirculation in the flow region. When the frequency of these vortex shedding matches the flexural resonance frequency of the hydrofoil the highly oscillating vibration occurs, named as singing (Blake et al. 1976). To minimize these problems recently, researchers at Sandia National Laboratories developed Marine and Hydrokinetic (MHKF) hydrofoils by providing finite thickness to the trailing edge of different hydrofoils of the NACA44 series. They assessed the performance of MHKF at a different angles of attack for non-cavitating flow using XFOIL and unsteady RANS solver named as OVERFLOW and found that hydrodynamic performance of MHKF hydrofoil is higher than NACA4418 for marine applications (Shiu et al. 2012). However, about MHKF, other relevant questions have not been reported yet, like how the performance of MHKF-180 is different from NACA4418 under cavitating conditions for various cavitation numbers and at a different angles of attack.

With this motivation, we present the computational analysis on MHKF-180 hydrofoil using the single fluid URANS method based on the equilibrium homogeneous mixture of two-phase flow in commercial software ANSYS Fluent. For cavitating flows, the Realizable $\kappa - \epsilon$ turbulence model been used along with the Zwart–Gerber–Belamri cavitation model. To establish our test procedure and to understand the physics of the cavitation process, initial simulation is conducted on NACA4412 hydrofoil at different angles of attack and at various cavitation numbers and results for this are validated with the results of experimental work (Kermeen 1956).

This paper is arranged in six sections. In Sect. 2, the complete description of hydrofoil terminology is given. In Sect. 3, we present the mathematical formulation defining governing equations, turbulence model equations and cavitation model equations. In Sect. 4, we discussed the computational domain, grid generation and boundary conditions. In Sect. 5, we validated our model and evaluated the performance of MHKF-180 hydrofoil and compared it with NACA4418. Section 6 finally concludes the paper with new findings and brief summary.

2 MHKF-180 and NACA4418 hydrofoil profiles

Figure 1 shows the 2-D profiles of NACA4412, NACA4418 and MHKF-180 hydrofoils. Here, NACA4412 hydrofoil is described as having maximum camber of 4% located at 40% of chord from the leading edge with the maximum thickness of 12% of the chord. Similarly, NACA4418 has the maximum camber of 4% located at 40% (0.4 chords) from the leading edge with the maximum thickness of 18% of the chord. Both the NACA4412 and NACA4418 have the sharp trailing edge.

MHKF-180 (Marine Hydrokinetic Foil) is the modified NACA4418 hydrofoil having maximum camber of 4% located at 40% of the chord length and having maximum thickness of 18% of the chord with finite thickness of 1.88 mm at the trailing edge as shown in Fig. 1.

3 Mathematical formulation

3.1 Governing equations

The most common model used to solve the cavitating flow is the homogeneous mixture model. In this model, the pressure, temperature, and velocity between the phases are considered to be equal. The justification is given by assuming that the mass and momentum transfer is fast enough to reach equilibrium (Hanimann et al. 2016). The governing equations for this mixture model involve solving the unsteady Reynold's Navier–Stokes (URANS) equations using the turbulence model. The URANS equations for two-phase flow (Saha 2014), are expressed as below:

$$\frac{\partial \rho_{\mathrm{m}}}{\partial t}+\frac{\partial\left(u_j \rho_{\mathrm{m}}\right)}{\partial x_j}=0, \tag{1}$$

$$\frac{\partial\left(\rho_{\mathrm{m}} u_i\right)}{\partial t}+\frac{\partial\left(\rho_{\mathrm{m}} u_i u_j\right)}{\partial x_j}=-\frac{\partial p}{\partial x_i} +\frac{\partial\left[\mu_{\mathrm{eff}}\left(\frac{\partial u_i}{\partial x_j}+\frac{\partial u_j}{\partial x_i}-\frac{2}{3} \frac{\partial u_i}{\partial x_i}\right)\right]}{\partial x_j}, \tag{2}$$

where ρ_{m} is the fluid mixture density,u_i is the Reynold's averaged velocity, p is the local static pressure, μ_{eff} is the effective viscosity and it is expressed as $\mu_{\mathrm{eff}}=\mu+\mu_{\mathrm{t}}$, where μ is the molecular viscosity and μ_{t} is the turbulent viscosity which is modelled using different turbulence model. For $\kappa-\epsilon$ turbulence model μ_{t} is expressed as:

$$\mu_{\mathrm{t}}=\rho_{\mathrm{m}} C_\mu \frac{\kappa^2}{\epsilon} \tag{3}$$

where κ is the turbulent kinetic energy, ϵ is the rate of dissipation of kinetic energy and C_μ is the model parameter for which required details are given later in Sect. 3.2. In the above equation, ρ_{m} is calculated using different cavitation models and it is related to the vapor volume fraction α_{v}, to vapor density ρ_{v}, and to liquid density ρ_{l} as:

$$\rho_{\mathrm{m}}=\alpha_{\mathrm{v}} \rho_{\mathrm{v}}+\left(1-\alpha_{\mathrm{v}}\right) \rho_{\mathrm{l}} \tag{4}$$

3.2 Turbulence model

There are various models available which are used to solve the turbulent viscosity (μ_{t}) like standard $\kappa-\epsilon$ model, RNG $\kappa-\epsilon$ model, Realizable $\kappa-\epsilon$ model, standard $\kappa-\omega$ model, SST $\kappa-\omega$ model etc. However, in cavitating flows, the Realizable $\kappa-\epsilon$ model found to be more effective than other models (Shih et al. 1995). The modelled transport equations for turbulent kinetic energy (κ) and its rate of dissipation (ϵ) for Realizable $\kappa-\epsilon$ model are (Shih et al. 1995):

$$\frac{\partial\left(\rho_{\mathrm{m}} \kappa\right)}{\partial t}+\frac{\partial\left(\rho_{\mathrm{m}} \kappa u_j\right)}{\partial x_j}=\frac{\partial\left[\left(\mu+\frac{\mu_{\mathrm{t}}}{\sigma_\kappa}\right) \frac{\partial \kappa}{\partial x_j}\right]}{\partial x_j} +G_\kappa-\rho_{\mathrm{m}} \epsilon-Y_M \tag{5}$$

$$\frac{\partial\left(\rho_{\mathrm{m}} \epsilon\right)}{\partial t}+\frac{\partial\left(\rho_{\mathrm{m}} \epsilon u_j\right)}{\partial x_j}=\frac{\partial\left[\left(\mu+\frac{\mu_{\mathrm{t}}}{\sigma_\epsilon}\right) \frac{\partial \epsilon}{\partial x_j}\right]}{\partial x_j} -\rho_{\mathrm{m}} C_2 \frac{\epsilon^2}{\kappa+\sqrt{\nu \epsilon}} \tag{6}$$

where G_κ is the turbulent kinetic energy due to the mean velocity gradients, Y_M is the contribution of the fluctuating dilatation in compressible turbulence to the overall dissipation rate, $C_2=1.9$, $\sigma_\kappa=1.0$ and $\sigma_\epsilon=1.2$ are the model constants. Realizable $\kappa-\epsilon$ model does not assumes C_μ as constant as it is accepted in other $\kappa-\epsilon$ models rather, it varies according to the flow field to satisfy the physics of turbulent flows (Reynolds 1987).

3.3 Cavitation model

In Eq. (4), the vapor volume fraction (α_{v}) on the hydrofoil can be determined using various cavitation models. These models are Singhal et al., Schnerr–Sauer model and Zwart–Gerber–Belamri cavitation model. Based on internal assessment we found that for such type of applications both Schnerr-Sauer

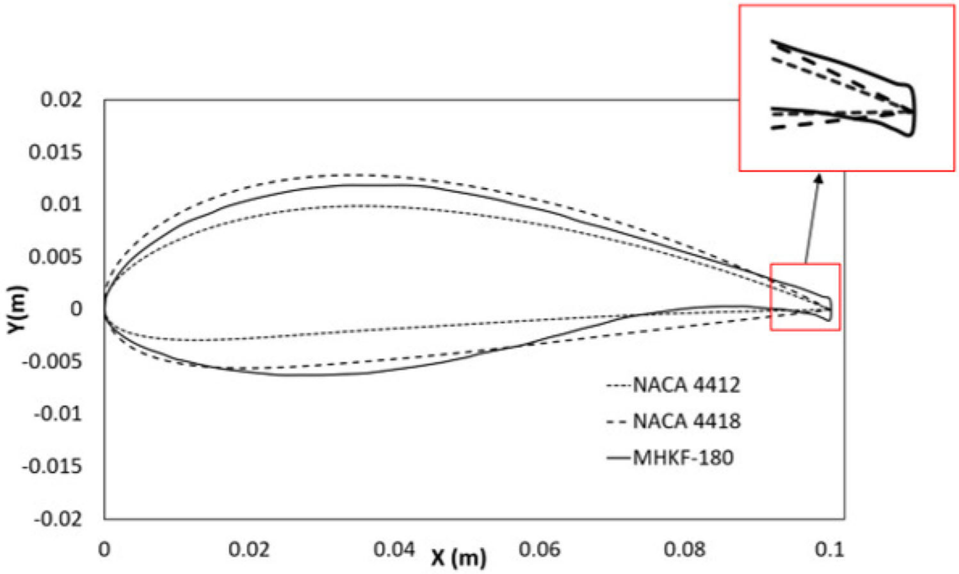

Fig. 1 NACA4412, NACA4418 and MHKF-180 profiles (Shiu et al. 2012)

model and Zwart–Gerber–Belamri model are giving close results but people in the literature have preferred Zwart–Gerber–Belamri model (Saha 2014; Niedźwiedzka 2017). Hence, Zwart–Gerber–Belamri cavitation model is used to determine the vapor volume fraction. The transport equation for this model is given as (Niedźwiedzka 2017):

$$\frac{\partial\left(\alpha_{\mathrm{v}}\rho_{\mathrm{v}}\right)}{\partial t}+\frac{\partial\left(u_j\rho_{\mathrm{v}}\alpha_{\mathrm{v}}\right)}{\partial x_j}=R_{\mathrm{e}}-R_{\mathrm{c}} \tag{7}$$

where R_e and R_c are the source terms related to evaporation and condensation of vapor bubbles, respectively. For Zwart–Gerber–Belamri model source term are given as:

$$R_{\mathrm{e}}=F_{\mathrm{vap}}\frac{3\alpha_{\mathrm{nuc}}\left(1-\alpha_{\mathrm{v}}\right)\rho_{\mathrm{v}}}{R_{\mathrm{b}}}\sqrt{\frac{2}{3}\frac{\left(p-p_{\mathrm{sat}}\right)}{\rho_{\mathrm{l}}}} \tag{8}$$

$$R_{\mathrm{c}}=-F_{\mathrm{cond}}\frac{3\alpha_{\mathrm{v}}\rho_{\mathrm{v}}}{R_{\mathrm{b}}}\sqrt{\frac{2}{3}\frac{\left(p_{\mathrm{sat}}-p\right)}{\rho_{\mathrm{l}}}} \tag{9}$$

where R_b is the radius of bubble, p_{sat} is the saturation pressure of the liquid, F_{vap} and F_{cond} are the evaporation and condensation coefficients having values 50 and 0.001, respectively. For Zwart–Gerber–Belamri the bubble radius ($R_b = 10^{-6}$ m) and $\alpha_{nuc} = 5\times10^{-4}$.

3.4 Variables of interest

There are various non-dimensional parameters that define the hydrodynamic performance of hydrofoil, like cavitation number (σ), pressure coefficient (C_p), lift coefficient (C_l) and drag coefficient (C_d). The cavitation number (σ) is a non-dimensional number that determines the cavity formation on the hydrofoil. It is expressed as the ratio of the difference between local absolute pressure and fluid vapor pressure to the dynamic pressure (Brennen 2014).

$$\sigma=\frac{p-p_{\mathrm{v}}}{\frac{1}{2}\rho U_{\infty}^{2}}; \tag{10}$$

where, U_∞ is the free-stream velocity (m/s), ρ is the density of water (kg/m^3), p_∞ is the pressure at freestream condition (Pa), p is the local static pressure (Pa), and p_v is the vapor pressure of the liquid (Pa).

The pressure coefficient (C_p) is defined as the ratio of the pressure difference on the hydrofoil to the dynamic pressure which is given by

$$C_{\mathrm{p}}=\frac{p-p_{\infty}}{\frac{1}{2}\rho U_{\infty}^{2}}. \tag{11}$$

The negative and the positive values of (C_p) indicates the suction surface and pressure surface respectively, while the maximum value of (C_p) is obtained as unity at the leading edge (Abbott and Von Doenhoff 2012). The difference in pressure on the suction and the pressure side results in the net upward force which is known as lift force. In non-dimensional form the lift force is represented by the lift coefficient given as (C_l). Similarly, there is resistive force developed in the opposite direction of fluid flow known as drag force, which is quantified using non-dimensional number (C_d) which is given by:

$$C_{\mathrm{l}}=\frac{\text{Lift}}{\frac{1}{2}\rho AU_{\infty}^{2}}; \tag{12}$$

$$C_{\mathrm{d}}=\frac{\text{Drag}}{\frac{1}{2}\rho AU_{\infty}^{2}}; \tag{13}$$

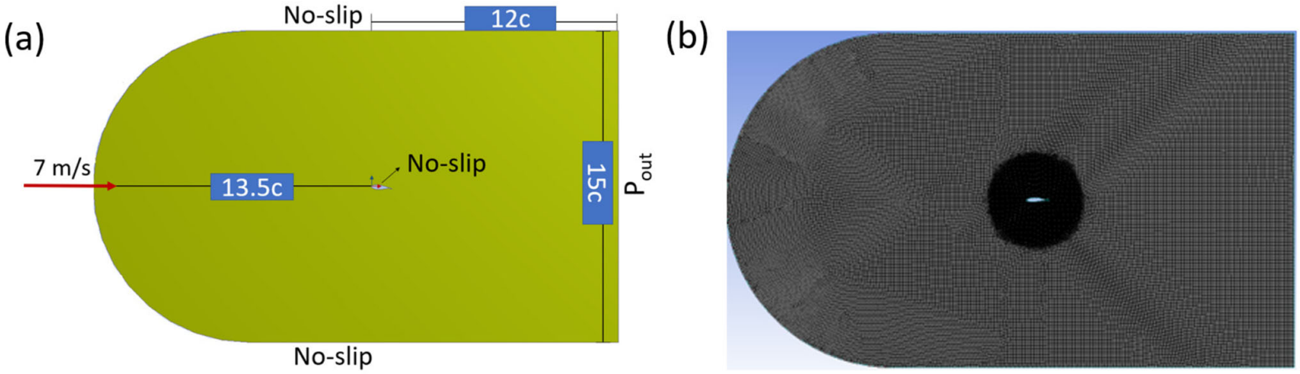

Fig. 2 **a** Computational domain dimensions and **b** meshing around NACA4412, $\alpha = 8°$

where A is the area of the hydrofoil (m^2).

4 Grid generation and boundary conditions

4.1 Computational domain and grid generation

Two-dimensional cambered NACA4412, NACA4418 and MHKF-180 hydrofoils having 0.1 m chord length (c) are simulated using rectangular computational fluid domain. The inlet is C type inlet which provides the advantage of reduced computational cost as compared to rectangular type inlet (Berntsen et al. 2001; Ghadimi et al. 2018; Mokhtar and Zheng 2006; Huang et al. 2010; Karim and Ahmmed 2012) as shown in Fig. 2. The size of domain is taken as 25.5c in x-direction and 15c in y-direction. The dimension are chosen such that negligible effect of wall boundary conditions reflect on the flow near the hydrofoil (Procedures 2014). The inlet is having 7.5c radius located at 13.5c in the upstream and outlet is at 12c in downstream from the leading edge of hydrofoil.

The quadrilateral mesh elements are generated in the fluid domain as shown in Fig. 2. Quadrilateral elements are higher order elements that are always preferred for two-dimensional geometries for better results (ITTC and Procedures 2011). To capture the flow behaviour on the hydrofoil boundaries, the mesh around the hydrofoil is progressively refined within a circular region and more fine grids are used at the edges of the hydrofoil in the form of inflation layers as shown in Fig. 3. The inflation layer meshing is provided to accurately capture the boundary layer regions on the hydrofoil.

Since numerical results depend on the grids, we performed grid independence test using five different grid numbers: 50,000, 60,000, 70,000, 96,000 and 115,000. The results based on the grid independence test is discussed later in results and discussion Sect. 5.

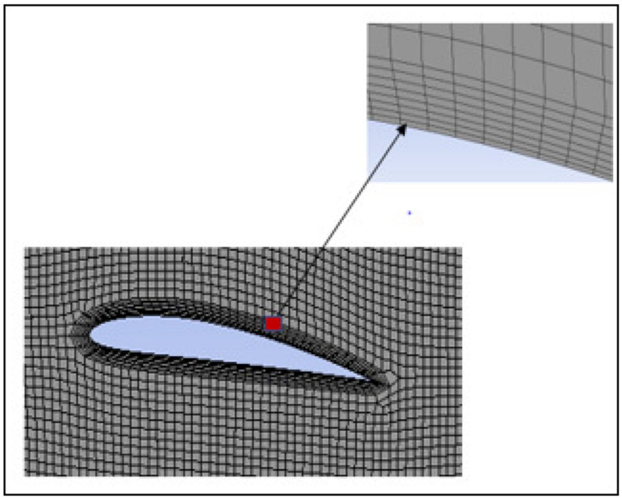

Fig. 3 Inflation layers around the hydrofoil, $\alpha = 8°$

4.2 Boundary conditions

A uniform x-component velocity of 7 m/s is specified at the inlet while the outlet pressure is specified based on the required cavitation numbers. The Reynold's number (Re) based on the inlet velocity and chord length is taken as 0.7×10^6. The hydrofoil edges and upper and lower walls of computational domain are set as no slip conditions. All these boundary conditions are shown in Fig. 2 and the reference values used are mentioned in Table 1.

The Realizable $\kappa - \epsilon$ turbulence model along with Zwart–Gerber–Belamri cavitation model are used in the simulation. For pressure and velocity coupling, the Coupled scheme is used. This scheme provides robust solutions by solving the pressure and momentum based continuity equations together. For pressure, we used PRESTO (Pressure Staggering Option) which requires no assumption for the pressure gradients and interpolation errors on the boundary as it solves the staggering pressure at the face of the control volume (ANSYS 2013). For volume fraction, momentum, turbulent dissipation rate

Table 1 Reference values

U_∞ = 7 m/s	c = 0.1 m
ρ_l = 998.2 kg/m^3	p_v = 3540 Pa
ρ_v = 0.5542 kg/m^3	$Re = 0.7\times10^6$
$\mu_l = 1\times10^{-3}$ Pa s	$\mu_v = 1.34\times10^{-5}$ Pa s

and turbulent kinetic energy QUICK (Quadratic Upstream Interpolation for Convective Kinetics) scheme is used which is higher-order differencing scheme.

5 Results and discussion

5.1 Grid independence test

To check the grid independency on the simulation results, we used different grid numbers on three hydrofoils i.e. NACA4412, NACA4418 and MHKF-180. In Fig. 4, we present the cases that we have simulated in this work. Case A has 50,000 grids, Case B has 60,000 grids, Case C has 70,000 grids, Case D has 96,000 grids and Case E has 115,000 grids. For determining the difference between C_l values of all the grids, percentage error is calculated with respect to the finest grid (E) as shown in the Table 2. The minimum percentage error for all three hydrofoils is found for grid D and values for the same are 0.067% for NACA4412, 0.356% for NACA4418 and 0.058% for MHKF-180. Similarly, in Fig. 5 cavity length convergence is presented with the help of pressure coefficient curve and cavity length on suction side of NACA4418 at 4° and $\sigma = 1$ for different number of grids. From Fig. 5a, we can clearly see that the pressure coefficient curve of 96,000 and 115,000 are almost overlapping each other. In Fig. 5b the cavity length value of 96,000 and 115,000 grid is equal. Based on this comparison Grid D is chosen for all other simulations. For the simulation we have also tested the result's dependency on the time step size for which three time step sizes are used i.e. 10^{-2} s, 10^{-3} s and 10^{-4} s. From the comparison (the results not shown here), we found that the time step 10^{-3} is sufficiently small to capture the flow physics. Hence, 10^{-3} has been selected as a time step for all the simulations. All the results presented are at an instant of 5 s while time-averaging is performed after 2 s i.e. when the flow has stabilised.

5.2 Validation of computational setup

To ensure the quality of the results generated by the numerical solution it is necessary to perform model validation. For this purpose, we compare our results with the experimental work by Kermeen (1956). Kermeen performed his experiment on NACA4412 hydrofoil at $Re = 0.7 \times 10^6$ for different angles of attack and at different cavitation numbers. Following Kermeen we simulated NACA4412 with varying $\alpha = 0°–16°$. The results are shown in Fig. 6

In Fig. 6, the lift coefficient results are compared at $\sigma = 1$ with changing angles of attack. Initially, with the increase in angle of attack, the pressure difference on the hydrofoil increases that results in increase of lift coefficient values. After attaining maximum value, the lift coefficient starts decreasing due to flow separation and formation of vortices on the hydrofoil. Figure 7 shows the comparison of vapor cavity formed on the NACA4412 hydrofoil at $\alpha = 8°$ for two different σ. The comparison is made with the Kermeen experimental work (Kermeen 1956). Clearly, from the above comparison, it can be concluded that our numerical results are reliable enough. Next we will evaluate the hydrodynamic performance of MHKF-180 and NACA4418 hydrofoils.

5.3 Hydrodynamic performance of MHKF-180 hydrofoil with respect to NACA4418 at different cavitation numbers

In Fig. 8, we present the time averaged lift coefficient of MHKF-180 and NACA4418 at α = 12° for cavitation numbers ranging from 0.6 to 3.5. Here, we see that there is gradual increase in the lift coefficient value with the increasing cavitation number. Further, at larger values of cavitation, we get an almost constant value of C_l. At lower cavitation number, vapor cavity forms and as a results there is decrease in pressure difference on the hydrofoil, leading to reduction in lift coefficient values. However, on further increase in σ the length of the vapor cavity decreases and so the C_l increases. After certain value of σ, the cavity disappears. At this point we get the maximum C_l which remains almost constant. From Fig. 8, we can see that for MHKF-180 constant C_l is obtained at σ >1.9 and for NACA4418 at σ >2.3.

On comparing C_l of MHKF-180 and NACA4418 we have observed that MHKF-180 gives higher C_l as compared to NACA4418 at lower σ whereas, NACA4418 gives higher C_l than MHKF-180 at higher σ when cavitation stops. Clearly, we can say that MHKF-180 performs better under cavitation.

In Fig. 9, we present the time-averaged drag coefficient for MHKF-180 and NACA4418 at α = 12° for cavitation number ranging from 0.6 to 3.5. Here, we see that initially with the increase in cavitation number the C_d increases until it attains the maximum value . Further, on increasing the σ results in decreasing drag coefficient. The drag force on 2D hydrofoil is the sum of the pressure drag and skin friction drag. The pressure drag is mainly due to the shape and size of the hydrofoil, more the thickness of the hydrofoil more is the pressure drag while, skin friction drag is due to the viscous drag (Anderson 2010). At lower cavitation number there is larger cavity length and therefore, lower skin friction

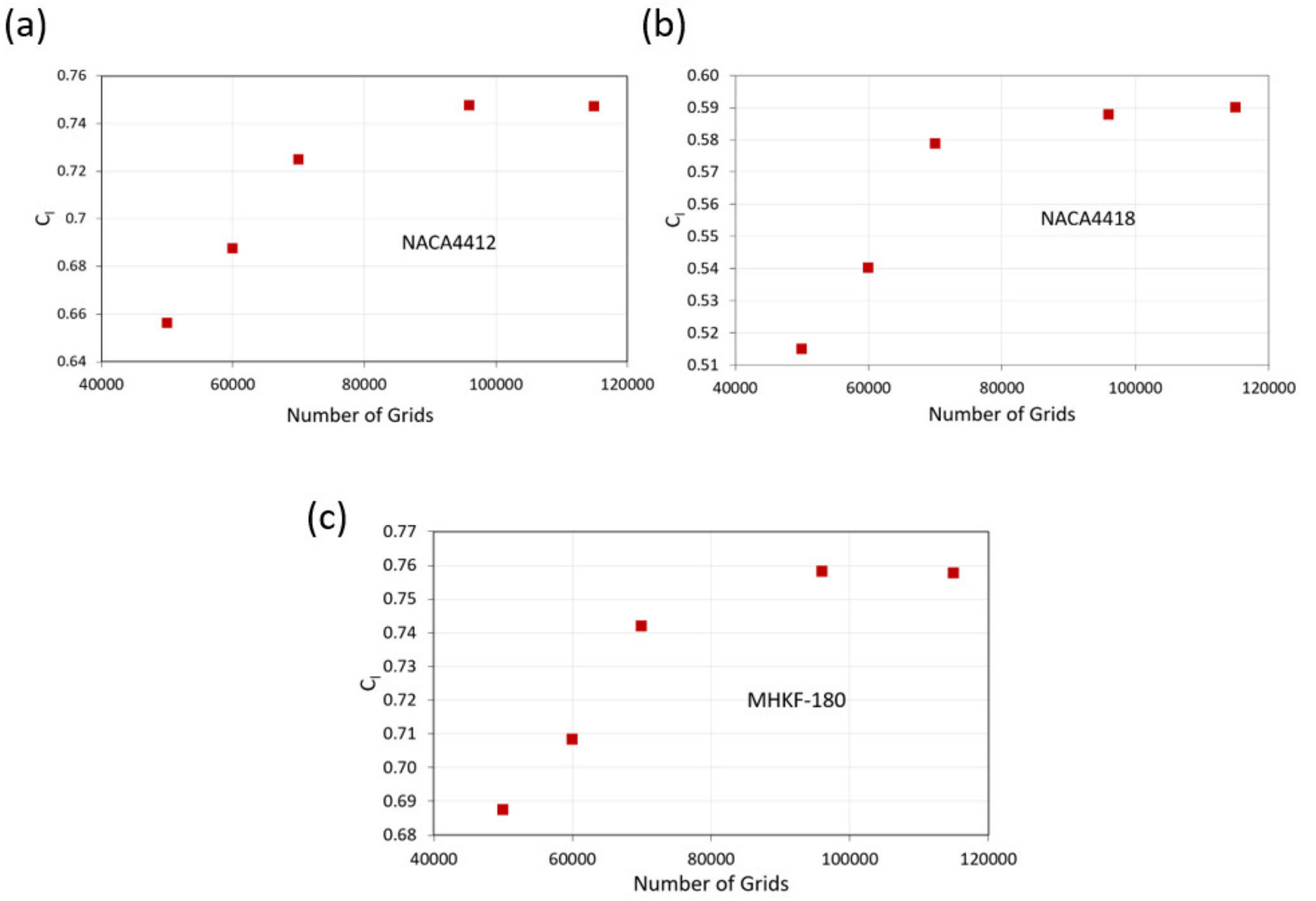

Fig. 4 Time averaged lift coefficient for **a** NACA4412, **b** NACA4418 and **c** MHKF-180 at different grid numbers

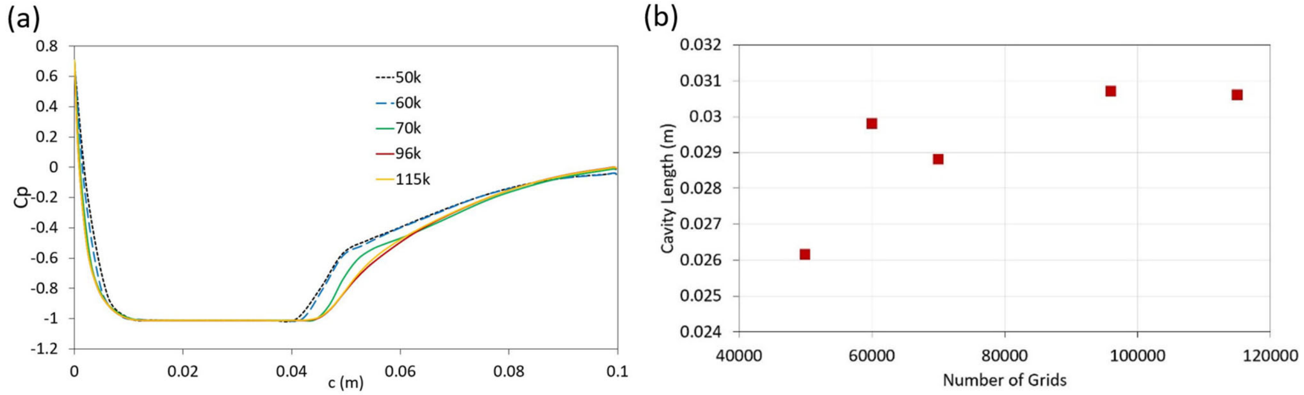

Fig. 5 Cp and cavity length on the suction surface of NACA4418 at $\alpha = 4°$ along different grid numbers

drag. But, as the cavitation number increases the skin friction drag also increases and at $\sigma = 1.1$, the drag force become maximum. After this value again with increase in cavitation number the drag coefficient decreases and at $\sigma = 2.3$, the C_d of both the hydrofoils become constant. By comparing the drag coefficient of MHKF-180 and NACA4418, we observed that for all value of σ the C_d of MHKF-180 is higher due to more pressure drag as a result of finite trailing edge thickness.

The other parameter for analysing the hydrodynamic performance of hydrofoil is lift to drag (l/d) ratio which is shown in Fig. 10. We can see that the l/d increases with increase in σ until it attains the maximum value at $\sigma = 2.3$ and beyond this the l/d value becomes constant. Though the two hydrofoils show different l/d with respect to σ, the l/d ratio can be seen to be close to each other for σ in the range 0.6–1.5. Since, C_l, C_d, l/d depends on angle of attack also, so in next

Table 2 Time averaged lift coefficients at different grid numbers

S. no.	No. of grids	Time-averaged lift coefficients, C_l			Percentage error relative to 115,000 grids (%)		
		NACA4412	NACA4418	MHKF-180	NACA4412	NACA4418	MHKF-180
A	50,000	0.6562	0.5149	0.6875	12.167	12.738	9.269
B	60,000	0.6875	0.5402	0.7084	7.978	8.448	6.502
C	70,000	0.7248	0.5789	0.7419	2.985	1.892	2.088
D	96,000	0.7476	0.5879	0.7581	0.067	0.356	0.058
E	115,000	0.7471	0.5900	0.7577	–	–	–

Fig. 6 Time averaged lift coefficient of NACA4412 hydrofoil for different angles of attack at $\sigma = 1$ (Kermeen 1956)

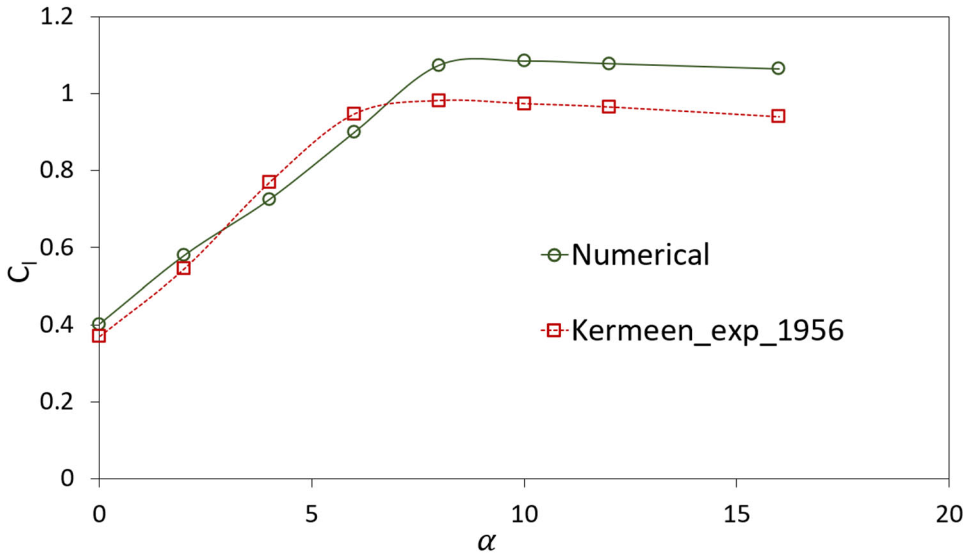

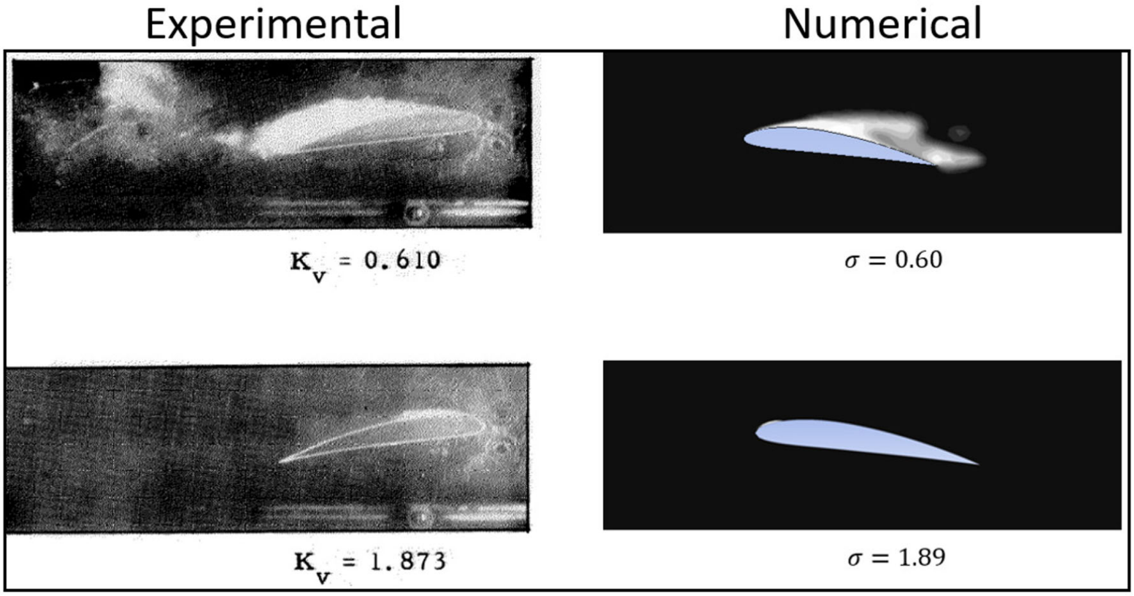

Fig. 7 Comparison of vapor volume fraction of present numerical work and experimental work (Kermeen 1956) on NACA4412 hydrofoil at $\sigma = 0.6$ and 1.8 for $\alpha = 8°$

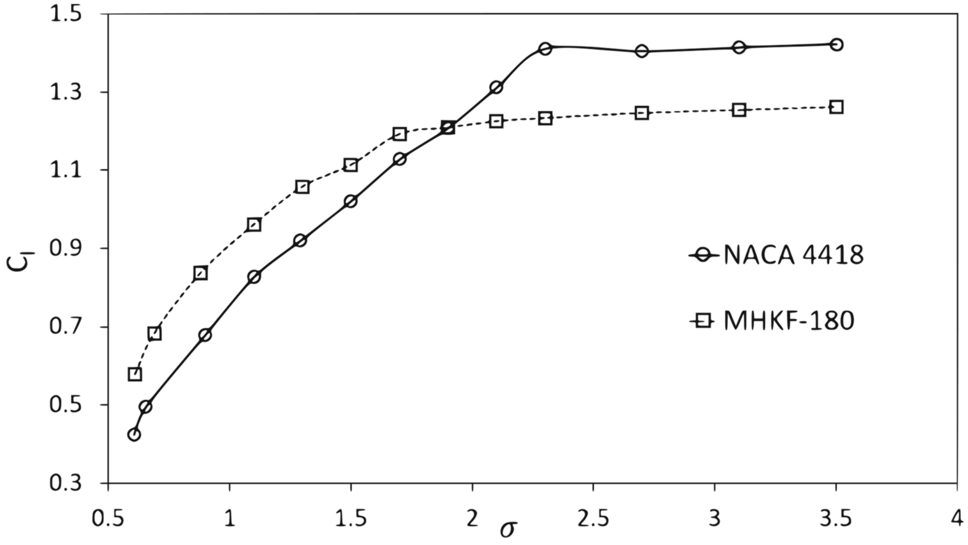

Fig. 8 C_l of MHKF-180 and NACA4418 at different cavitation numbers, σ

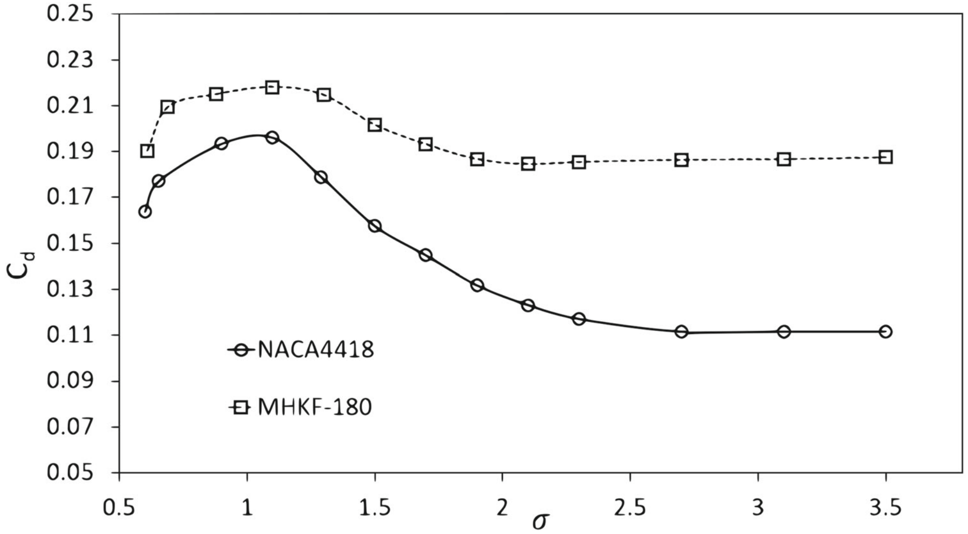

Fig. 9 C_d of MHKF-180 and NACA4418 at different cavitation numbers, σ

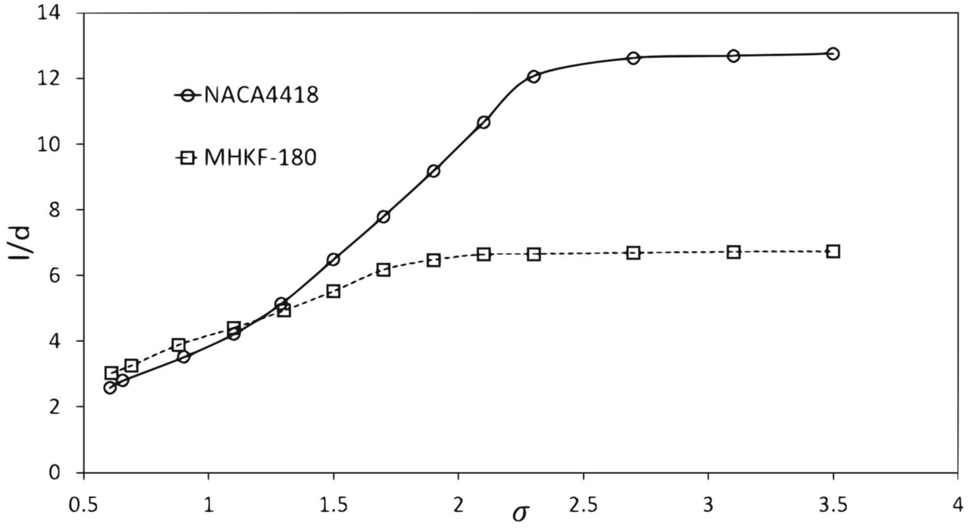

Fig. 10 l/d of MHKF-180 and NACA4418 at different cavitation numbers, σ

Fig. 11 C_l of MHKF-180 and NACA4418 at different angles of attack, α

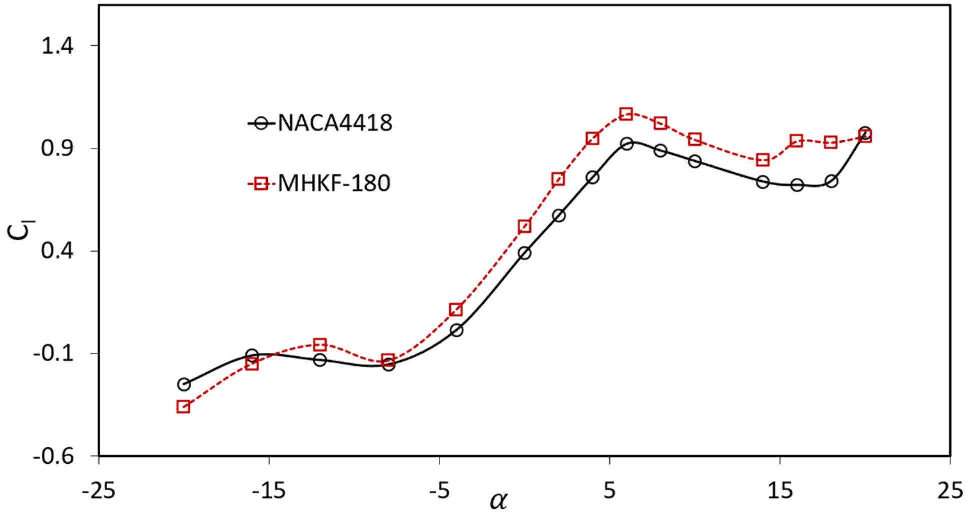

Fig. 12 C_d of MHKF-180 and NACA4418 at different angles of attack, α

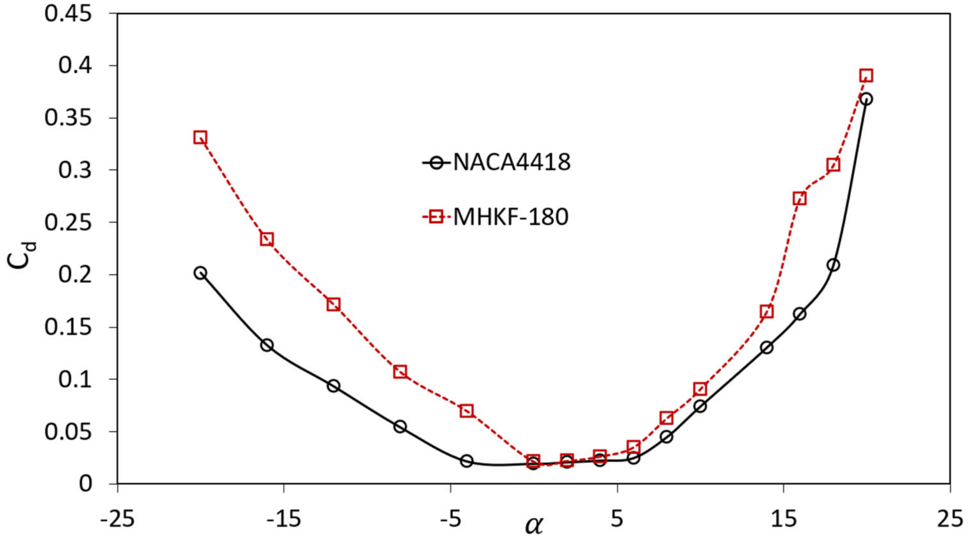

Fig. 13 l/d of MHKF-180 and NACA4418 at different angles of attack, α

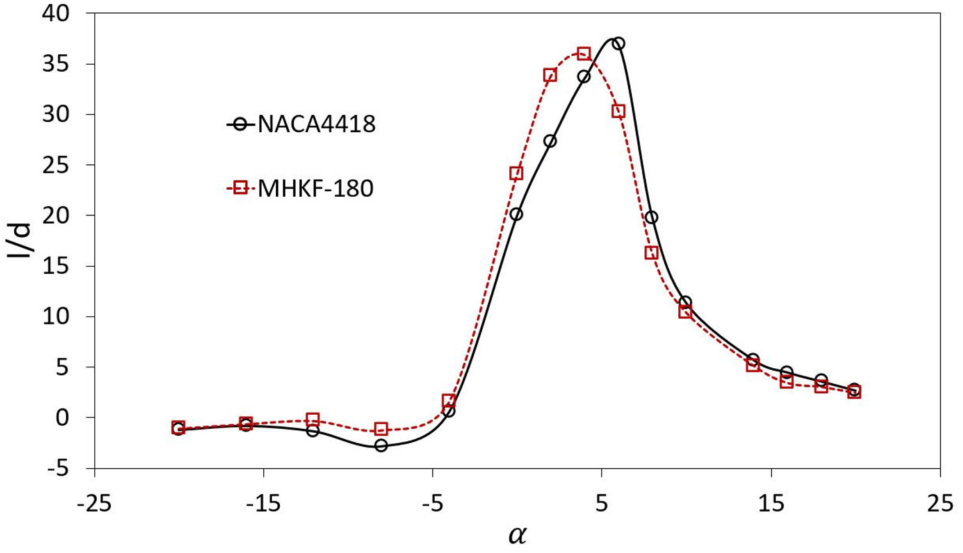

Fig. 14 Pressure coefficient and vapor fraction for NACA4418 and MHKF-180, σ = 1.5 and $\alpha = -20°$

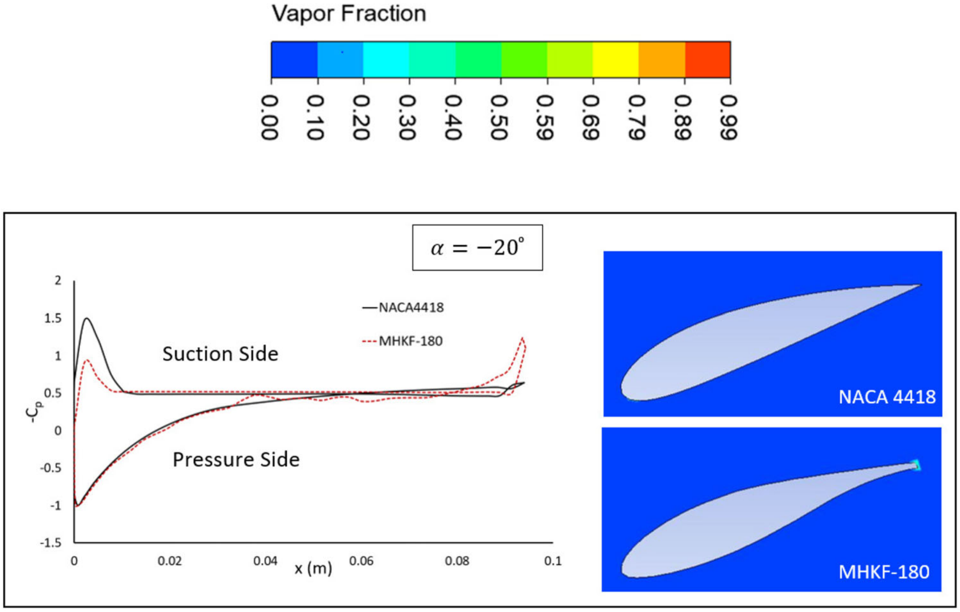

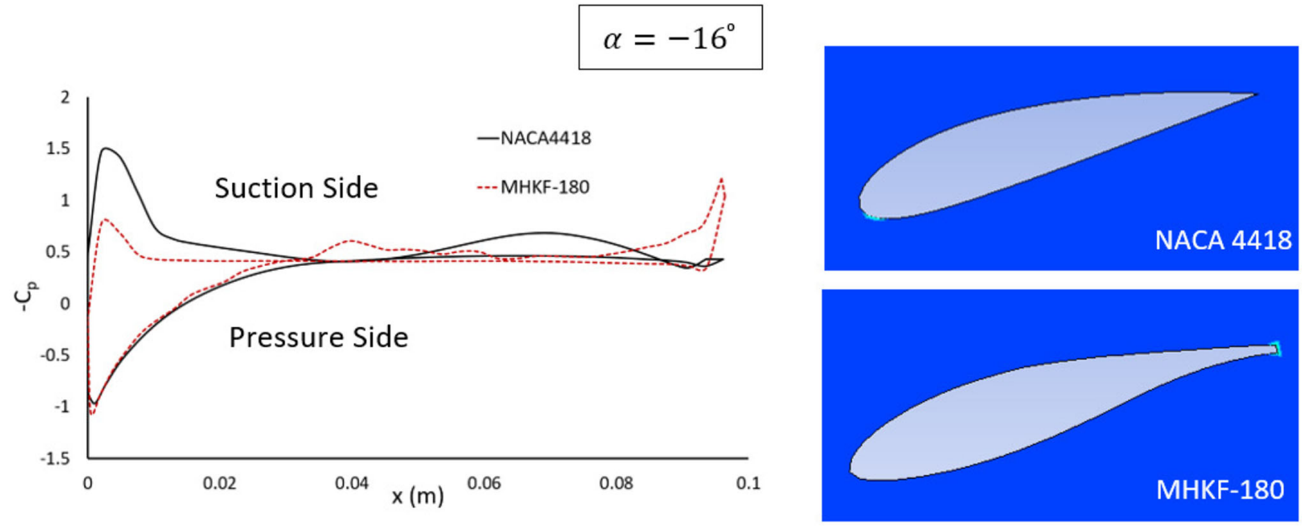

Fig. 15 Pressure coefficient and vapor fraction for NACA4418 and MHKF-180, σ = 1.5 and $\alpha = -16°$

section we investigate our quantities of interest at σ = 1.5 but at different angles of attack.

5.4 Hydrodynamic performance of MHKF-180 hydrofoil with respect to NACA4418 at different angle of attacks

In Fig. 11, we present the comparison of time-averaged lift coefficient of MHKF-180 and NACA4418 at angles of attack ranging from −20° to + 20° at σ =1.5. For negative α, we are getting negative values of C_l which is due to decrease in the pressure on the lower surface of the hydrofoil as compared to upper surface. At 0° C_l is not zero due to the fact that hydrofoils are cambered. For positive α the lift coefficient values are positive and at α = 6°, C_l is maximum i.e. 1.06 for MHKF-180 and 0.92 for NACA4418. The condition at which hydrofoil attains its maximum C_l is referred to as stall condition (Abbott and Von Doenhoff 2012; Anderson 2010). After α = 6°, C_l again starts decreasing due to reduction in pressure difference on the hydrofoil as a result of increasing flow separation and formation of vortices (Marchand et al. 2017). When we compare the performance of MHKF-180 and NACA4418, we found that MHKF-180 performs better for almost all angles of attack as it gives higher lift coefficient.

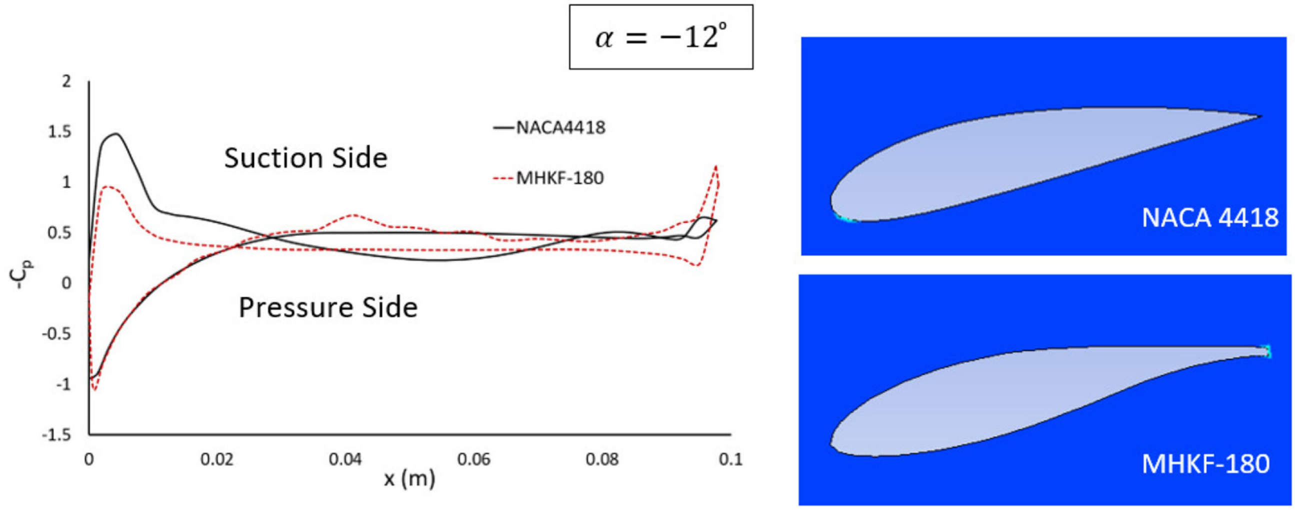

Fig. 16 Pressure coefficient and vapor fraction for NACA4418 and MHKF-180, σ = 1.5 and $\alpha = -12°$

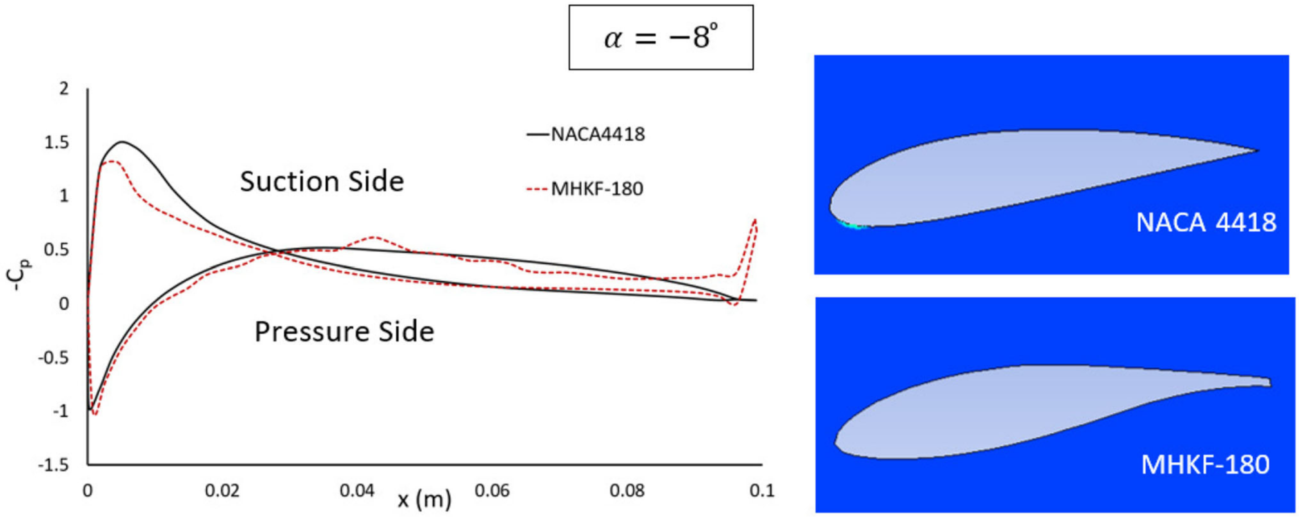

Fig. 17 Pressure coefficient and vapor fraction for NACA4418 and MHKF-180, σ = 1.5 and $\alpha = -8°$

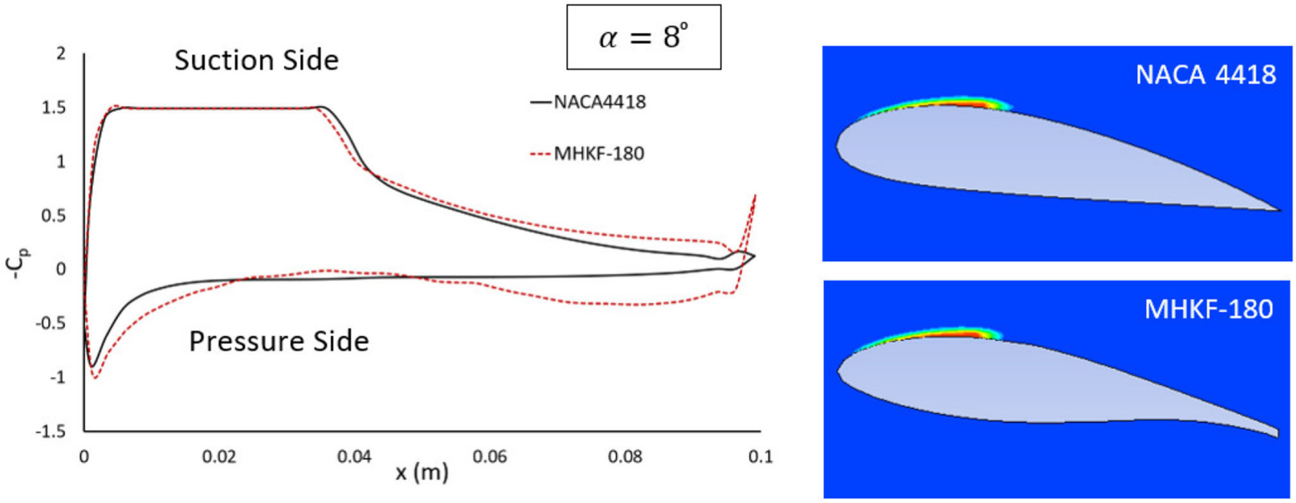

Fig. 18 Pressure coefficient and vapor fraction for NACA4418 and MHKF-180, σ = 1.5 and α = 8°

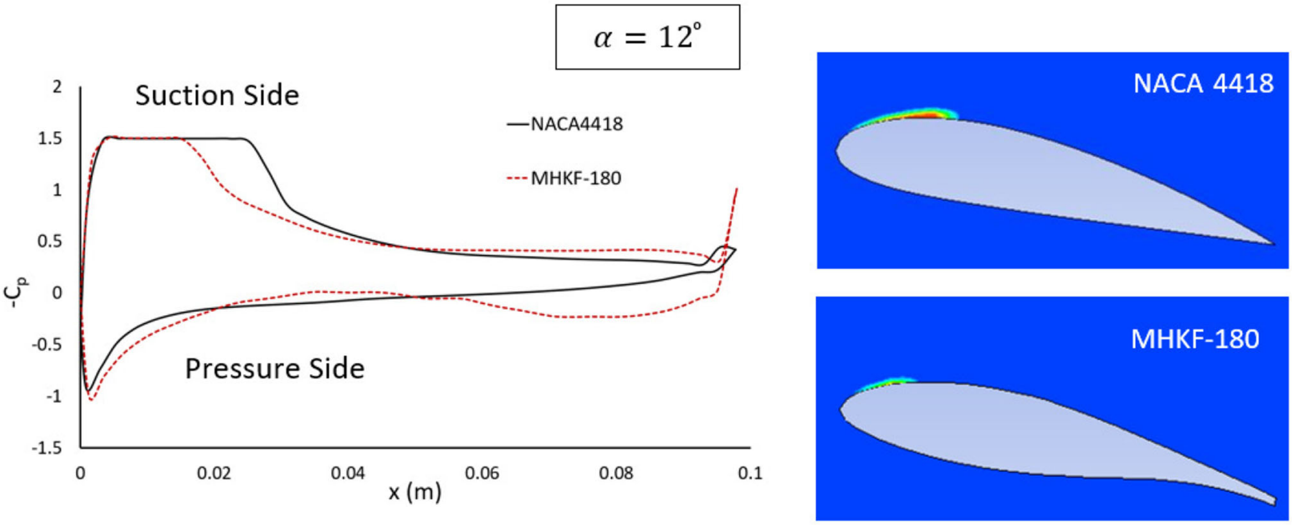

Fig. 19 Pressure coefficient and vapor fraction for NACA4418 and MHKF-180, σ = 1.5 and α = 12°

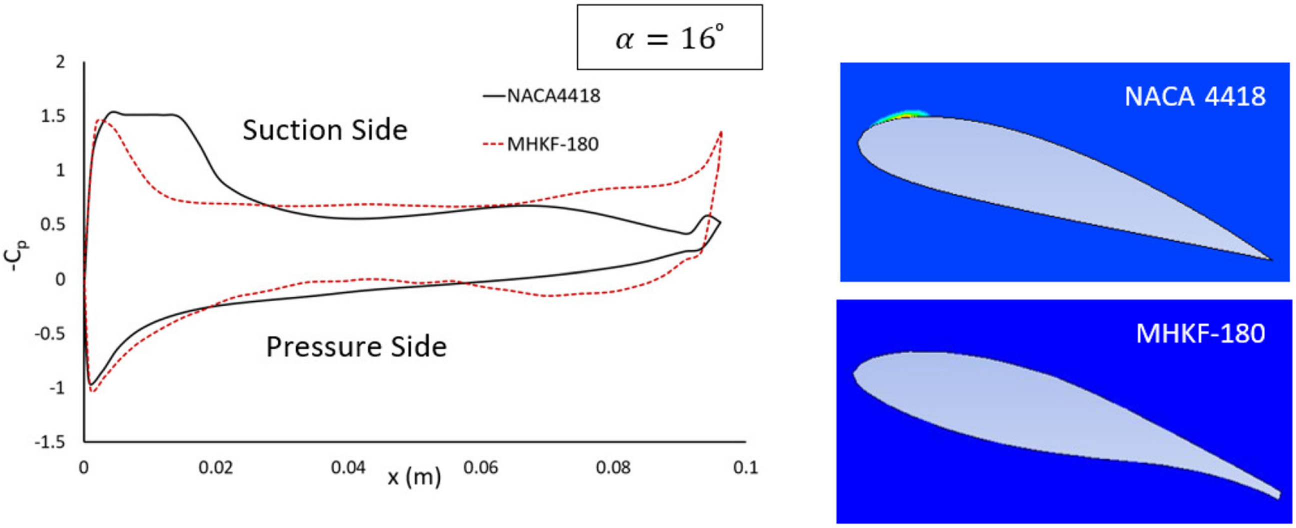

Fig. 20 Pressure coefficient and vapor fraction for NACA4418 and MHKF-180, σ = 1.5 and α = 16°

In Fig. 12, we show computed time-averaged drag coefficient of MHKF-180 and NACA4418 at different angles of attack ranging from −20° to + 20° for σ = 1.5. The C_d decreases with increase in α and attains minimum value and it remains constant till stall condition. After stall condition again it starts increasing. The minimum value of C_d is obtained at $\alpha = 0°$ for both the hydrofoils. The variation of C_d with respect to α is parabolic in nature which is consistent with the literature (Marchand et al. 2017; Abbott and Von Doenhoff 2012; Jones et al. 2015). On comparing the drag coefficient of MHKF-180 and NACA4418 hydrofoil for different angles of attack, we found that C_d of MHKF-180 is higher for all values of α due to increase in the thickness of the trailing edge.

In Fig. 13, we present the lift to drag ratio of hydrofoils at different angles of attack for σ =1.5. The l/d initially increases with the increasing angle of attack and reaches to maximum value. The maximum value of l/d is obtained at 4° for MHKF-180 and at 6° for NACA4418 hydrofoil after which lift to drag ratio decreases. By comparing the l/d of MHKF-180 and NACA4418, we found that for lower angles of attack the MHKF-180 has higher lift to drag ratio i.e. MHKF-180 performs better than NACA4418 hydrofoil below stall condition.

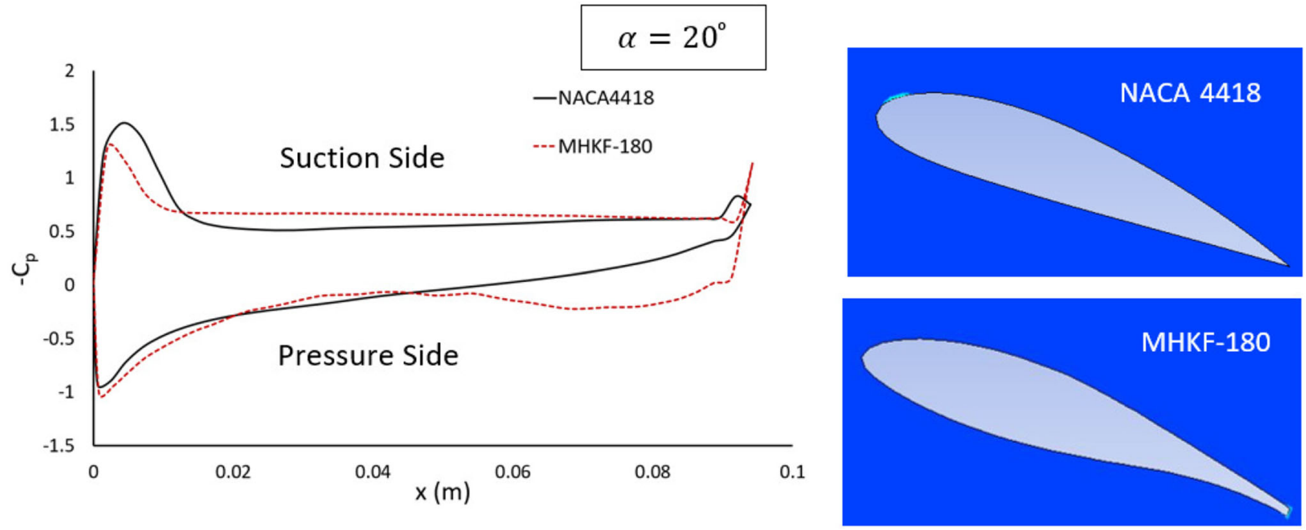

Fig. 21 Pressure coefficient and vapor fraction for NACA4418 and MHKF-180, σ = 1.5 and α = 20°

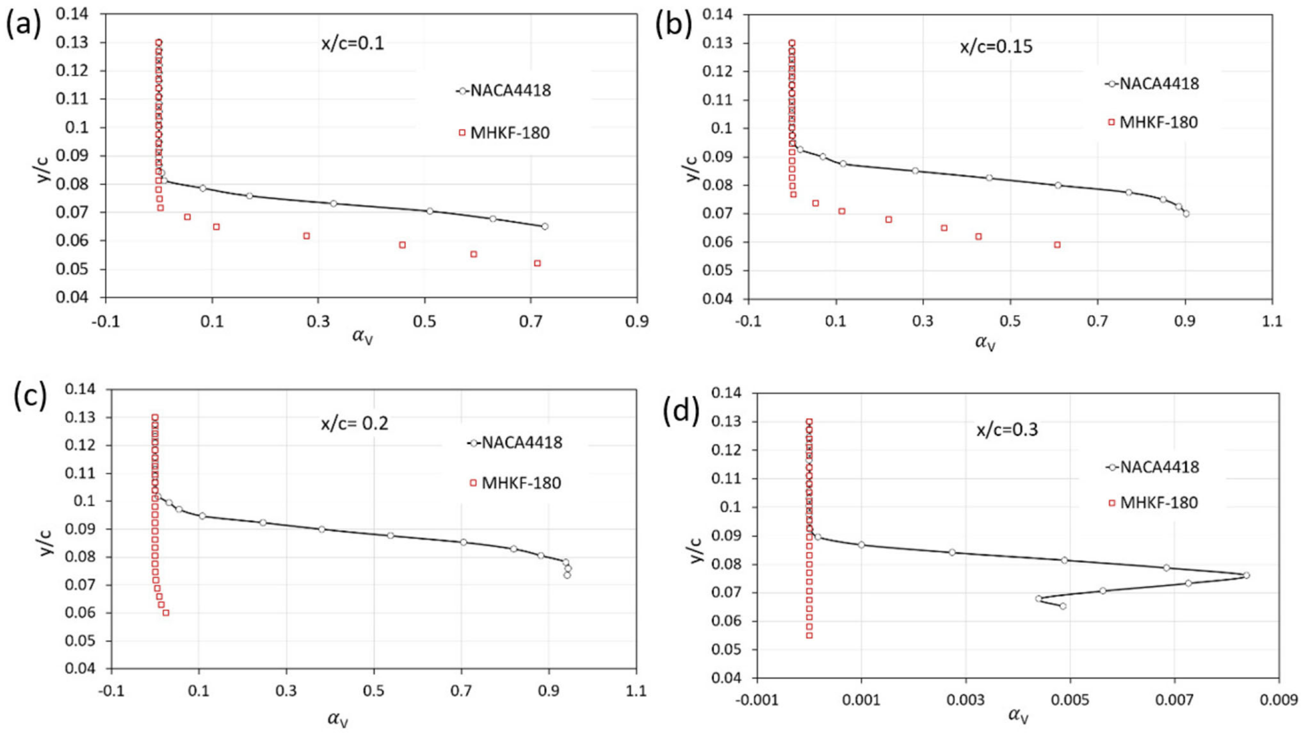

Fig. 22 Comparison of vapor volume fraction at **a** $x/c = 0.1$, **b** $x/c = 0.15$, **c** $x/c = 0.2$ and **d** $x/c = 0.3$ on MHKF-180 and NACA4418 hydrofoils at $\alpha = 12°$ and σ = 1.5

5.5 Pressure distribution, vapor volume fraction and velocity profiles on MHKF-180 and NACA4418 at different angles of attack

The pressure coefficient curves along with the vapor cavity on MHKF-180 and NACA4418 hydrofoils are shown in the Figs. 14, 15, 16, 17, 18, 19, 20 and 21 for different α at σ = 1.5. The pressure coefficient curve is an important parameter that tells about the pressure distribution on the hydrofoil and helps us to understand the formation of vapor cavity on the hydrofoil. As the suction side of the hydrofoil usually has lower pressure as compared to the pressure side, mainly cavitation takes place on the suction side. The constant value on the pressure coefficient curve indicates the cavity formation, and the length over which C_p remains constant is the length of cavity (Štigler and Svozil 2009; Huang et al. 2010;

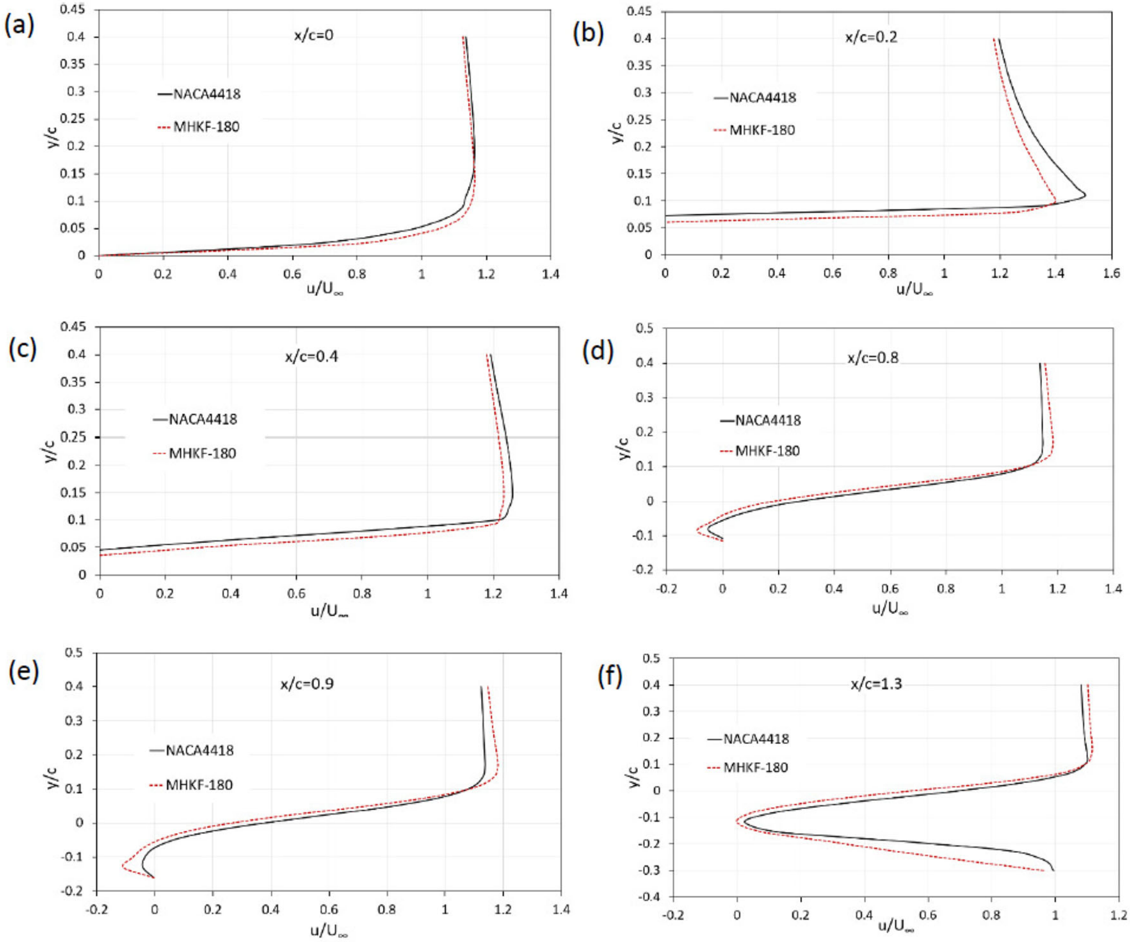

Fig. 23 Comparison of axial velocity profiles at **a** $x/c = 0$, **b** $x/c = 0.2$, **c** $x/c = 0.4$, **d** $x/c = 0.8$, **e** $x/c = 0.9$ and **f** $x/c = 1.3$ along the MHKF-180 and NACA4418 hydrofoils at $\alpha = 12°$ and $\sigma = 1.5$

Wu and Chen 2016). On analysing the cavitation on both the hydrofoils, we found that for negative angles of attack the NACA4418 has negligible cavity whereas, MHKF-180 has small cavity on the trailing edge with vapor fraction in range of 0.1-0.2. For positive angles there is no cavity formation for both the hydrofoils upto 4° and after 10° it starts decreasing again. Hence, largest cavity length is observed at 8° for both MHKF-180 and NACA4418 hydrofoil. Overall on comparing the pressure coefficient curves and vapor volume fraction, we found that MHKF-180 has a smaller cavity length as compared to NACA4418, and therefore MHKF-180 is less prone to cavitation at $\sigma = 1.5$.

For better understanding of the cavity formation on the hydrofoils, we have drawn vapor volume fraction on the normalized vertical lines at different chord-based locations ($x/c = 0.1$, 0.15, 0.2, and 0.3) at $\alpha = 12°$ and $\sigma = 1.5$ which is shown in Fig. 22. The maximum vapor fraction is observed near the leading edge on both the hydrofoils at $x/c = 0.1$ and as we move towards $x/c = 0.3$, the cavity on the MHKF-180 hydrofoil starts decreasing and becomes negligible at $x/c =$ 0.3. Therefore, we can say that at this particular value of σ, MHKF-180 is having smaller cavity length as compared to NACA4418.

The comparison of normalized x-component velocity profiles on MHKF-180 and NACA4418 hydrofoils along the vertical lines drawn on the suction side at six different chord-based locations, i.e. $x/c = 0$, 0.2, 0.4, 0.8, 0.9 and 1.3 are presented in Fig. 23, for 12° angle of attack at $\sigma = 1.5$. The positive velocity gradient represents that flow is attached to the hydrofoil surface, while the negative value represents the flow separation. It is observed that flow remains attached to both the hydrofoils till 0.4c as shown at location $x/c = 0$, 0.2, 0.4 after which reverse flow takes place causing negative velocity gradients as shown at $x/c = 0.8$, 0.9. Similarly, at $x/c = 1.3$ as the fluid leaves the hydrofoil surface there is reverse flow due to the formation of vortices near the trailing edge causing larger negative velocity gradients. The thicker the cavity in the chordwise direction, the larger is the velocity gradient in the normal direction (Hong et al. 2017). The maximum difference between the velocity profiles of both the hydrofoils is observed at $x/c = 0.2$, as MHKF-180 is having the lower vapor fraction as compared to NACA4418 which can also be visualised from the vapor fraction contour as shown in Fig. 19.

6 Conclusions

In this paper, we have studied the hydrodynamic performance of MHKF-180 and NACA4418 hydrofoil under cavitation in terms of lift coefficient, drag coefficient, pressure distribution and vapor volume fraction. For this purpose, we have performed simulation on 2D hydrofoils at various angles of attack and for different cavitation numbers. The turbulence effect is solved using Realizable $\kappa - \epsilon$ model and vapor volume fraction is calculated using Zwart–Gerber–Belamri cavitation model. Based on the results, the major findings are as follows:

(a) for lower values of cavitation number, the MHKF-180 hydrofoil is having higher lift coefficients as compared to NACA4418 and hence performing better.
(b) for different angle of attack the lift coefficient values of MHKF-180 hydrofoil is more as compared to NACA4418 hydrofoil under cavitating condition
(c) for $\sigma = 1.5$, the MHKF-180 is less prone to cavitation as it is having lower vapor fraction than NACA4418 at different values of α.
(d) the addition of thickness to the trailing edge of MHKF-180 hydrofoil results in an increase of drag coefficient both for different angles of attack and at different cavitation numbers.

The above mentioned results are presented for cavitation phenomenon on the 2D hydrofoils using URANS but the real effect of cavitation on the hydrofoil can be understood by studying two-way Fluid Structure Interaction (FSI) on hydrofoils and we hope to present the analysis of FSI on hydrofoils in our future work.

References

Abbott IH, Von Doenhoff AE (2012) Theory of wing sections: including a summary of airfoil data. Dover Publications, New York

Anderson JD Jr (2010) Fundamentals of aerodynamics. Tata McGraw-Hill Education, New York

ANSYS (2013) ANSYS Fluent 12 User‘s Guide. Release 12.0, ANSYS, Inc. Canonsburg, PA, USA

Berntsen GS, Kjeldsen M, Arndt RE (2001) Numerical modeling of sheet and tip vortex cavitation with FLUENT 5. In: Fourth international symposium on cavitation, NTNU, pp 1–8

Billet M, Holl J (1981) Scale effects on various types of limited cavitation. Trans ASME J Fluids Eng 103:405–14

Blake W, Maga L, Finkelstein G (1976) On the singing of hydrofoils. J Acoust Soc Am 59(S1):S20

Brennen CE (2014) Cavitation and bubble dynamics. Cambridge University Press, New York

Fabula A (1962) Thin-airfoil theory applied to hydrofoils with a single finite cavity and arbitrary free-streamline detachment. J Fluid Mech 12(2):227–240

Furuya O (1975) Three-dimensional theory on supercavitating hydrofoils near a free surface. J Fluid Mech 71(2):339–359

Ghadimi P, Tanha A, Tavakoli S, Feizi Chekab MA (2018) RANS simulation of the tip vortex flow generated around a NACA 0015 hydrofoil and examination of its hydrodynamic characteristics. J Mar Eng Tech 17(2):106–119

Hanimann L, Mangani L, Casartelli E, Widmer M (2016) Cavitation modeling for steady-state CFD simulations. In: 28th IAHR symposium on hydraulic machinery and systems (IAHR 2016): IOP conference series: earth and environmental science, Grenoble, France, vol 49, p 092005

Hong F, Yuan J, Zhou B, Li Z (2017) Modeling of unsteady structure of sheet/cloud cavitation around a two-dimensional stationary hydrofoil. Proc Inst Mech Eng Part E J Process Mech Eng 231(3):455–469

Huang S, He M, Wang C, Chang X (2010) Simulation of cavitating flow around a 2-D hydrofoil. J. Mar. Sci. Appl. 9(1):63–68

ITTC RP, Procedures R (2011) Guidelines: practical guidelines for ship CFD applications. ITTC Rep 7:02–03

Jones R, Cleaver D, Gursul I (2015) Aerodynamics of biplane and tandem wings at low Reynolds numbers. Exp Fluids 56(6):124

Karim MM, Ahmmed MS (2012) Numerical study of periodic cavitating flow around NACA0012 hydrofoil. Ocean Eng 55:81–87

Kermeen RW (1956) Water tunnel tests of NACA 4412 and Walchner Profile 7 hydrofoils in non cavitating and cavitating flows. Tech. rep 47-5, Hydrodynamics Laboratory, California Institute of Technology, California

Kinnas SA, Fine NE (1993) A numerical nonlinear analysis of the flow around two-and three-dimensional partially cavitating hydrofoils. J Fluid Mech 254:151–181

Kubota A, Kato H, Yamaguchi H (1992) A new modelling of cavitating flows: a numerical study of unsteady cavitation on a hydrofoil section. J Fluid Mech 240:59–96

Lohrberg H, Stoffel B, Fortes-Patella R, Coutier-Delgosha O, Reboud J (2002) Numerical and experimental investigations on the cavitating flow in a cascade of hydrofoils. Exp Fluids 33(4):578–586

Marchand J-B, Astolfi JA, Bot P (2017) Discontinuity of lift on a hydrofoil in reversed flow for tidal turbine application. Eur J Mech B Fluids 63:90–99

Mokhtar XDIKK, Zheng WA (2006) Aerodynamics and flow control of flapping wings. In: 44th AIAA Aerospace Sciences Meeting, vol 17, pp 12722–12731

Niedźwiedzka A (2017) Homogeneous cavitation modeling-analysis of basics of mathematical formulation of source terms. Modelowanie Inżynierskie 34:75–82

Phillips R, Fontaine AA, Straka WA, Jonson ML, van Dam C, Shiu H, Barone MF, Johnson E (2012) Cavitation testing of a specifically designed marine hydrokinetic turbine hydrofoil. Tech. rep., Sandia National Lab.(SNL-NM), Albuquerque, NM (United States)

Procedures I-R (2014) Practical guidelines for ship CFD applications. In: Proceedings of 26th ITTC, Hague, vol 20, pp 395–429

Reynolds W (1987) Fundamentals of turbulence for turbulence modeling and simulation. Tech. rep., Stanford Univ CA Dept of Mechanical Engineering

Saha K (2014) Modelling of cavitation in nozzles for diesel injection applications. Ph.D. Thesis, University of Waterloo, Ontario, Canada

Shih T, Liou W, Shabbir A, Yang Z, Zhu J (1995) A new $k-epsilon$ eddy viscosity model for high Re turbulent flow-model development and validation. Comput Fluids 24(3):227–238

Shiu H, Van Dam C, Johnson E, Barone M, Phillips R, Straka W, Fontaine A, Jonson M (2012) A design of a hydrofoil family for current-driven marine-hydrokinetic turbines. In: 20th international conference on nuclear engineering and the ASME 2012 power conference, Anaheim, California, USA, pp 839–847

Štigler J, Svozil J (2009) Modeling of cavitation flow on NACA 0015 hydrofoil. Eng Mech 16(6):447–455

Woods L (1964) On the theory of growing cavities behind hydrofoils. J Fluid Mech 19(1):124–136

Wu Y (1954) A theory for hydrofoils of finite span. J Math Phys 33(1–4):207–248

Wu P-C, Chen J-H (2016) Numerical study on cavitating flow due to a hydrofoil near a free surface. J Ocean Eng Sci 1(3):238–245